

IMPROVING THE CUBIC ZnS NANOCRYSTALS QUALITY BY SELF-ASSEMBLING INTO A MESOPOROUS STRUCTURE

S.V. NISTOR*¹, L.C. NISTOR¹, M. STEFAN, D. GHICA¹, C.D. MATEESCU¹, R. BIRJEGA²

¹National Institute of Materials Physics, P.O. Box MG-7, 077125 Magurele, Romania

²National Institute of Lasers, Plasma and Radiation Physics, P.O. Box MG-27, 077125 Magurele, Romania

E-mail: snistor@infim.ro

(Received August 28, 2009)

Abstract. Nanocrystals of cubic ZnS (cZnS) doped with 0.2 % mol Mn²⁺, self-assembled into a mesoporous structure, have been prepared at room temperature by a surfactant-assisted liquid-liquid reaction. The X-ray diffraction measurements confirm the formation of a sponge-like mesoporous structure built from ZnS nanocrystals with cubic (sphalerite) structure and pores of similar diameter of (1.8 ± 0.2) nm. The Transmission Electron Microscopy (TEM) images show that the mesoporous structure consists of nanocrystals of cZnS with a tight size distribution centered around the average diameter value (2.1 ± 0.3) nm. The analysis of the observed Electron Paramagnetic Resonance (EPR) spectrum demonstrates the presence of the Mn²⁺ activating ions at isolated sites in the mesoporous material, resulting in three types of paramagnetic centers called Mn²⁺(I), Mn²⁺(II) and Mn²⁺(III). The EPR spectrum of the Mn²⁺(I) center, attributed to substitutional Mn²⁺ ions at Zn²⁺ cation sites in the ZnS nanocrystals, exhibits the smallest linewidth values reported so far, reflecting an increased lattice ordering. The high quality of the nanocrystals forming the mesoporous cZnS:Mn, as reflected in a tight nanocrystallites size distribution and reduced crystallites lattice disorder, is attributed to the restraining effect of the self-assembling.

Key words: nanocrystals, self-assembling, mesoporous cZnS:Mn, electron paramagnetic resonance, transmission electron microscopy.

1. INTRODUCTION

The nanostructured wide band-gap semiconductors, doped with impurity ions are intensely investigated, due to the strong changes associated with the quantum confinement (QC) effect, which are expected to take place in their physical properties as the size of the component particles approaches the exciton Bohr radius [1]. In this respect, a large number of publications have been dedicated to the synthesis and characterization of the II-VI semiconducting, nanocrystalline ZnS doped with transition ions, which is well known for its outstanding optoelectronic properties [2]. Up to now, the results concerning the presence of the QC effect in

the optical properties of the most investigated Mn^{2+} doped nanocrystalline ZnS with cubic structure (cZnS:Mn), usually synthesized at low temperatures ($T < 350^\circ\text{C}$) from liquid solution, are contradictory, some authors attributing the observed changes to surface localization of the impurity ions and/or the effect of the additive which coats the nanocrystals [3]. In what concerns the localization of the Mn^{2+} activating ions in the nanocrystalline ZnS, the pertinent information is inferred mainly from Electron Paramagnetic Resonance (EPR) spectroscopy investigations. The results reported so far [4–7] exhibit a large spread in the spin Hamiltonian (SH) parameter values containing the essential information for determining the localization of the activating paramagnetic ions. Thus, it is difficult to decide if the various reported sets of SH parameters correspond to Mn^{2+} ions localized at sites with different local structure / coordination, or are just reflecting some large margins of errors while corresponding in fact to the same centers. The large variation in the reported SH parameters is largely related to the broad EPR spectrum component lines associated with the lower degree of crystallinity characteristic for nanocrystalline semiconductors [8]. It is therefore essential to be able to investigate nanocrystalline cZnS (and other II–VI semiconductor nanocrystals) with an improved lattice quality and a narrow size distribution, with narrower spectrum lines, which in turn would lead to the determination of more accurate spectrum parameter values, resulting in an improved understanding of the localization of the Mn^{2+} ions in the investigated material.

Compared to simple aggregates of nanocrystals, the self-assembled mesoporous nanostructures exhibit a larger surface area, higher chemical activity and a better stability [9, 10]. One would also expect the self-assembling to have a restraining effect on crystallites growth, resulting in a narrower size distribution of the nanocrystals and a better quality (crystallinity) of their lattice. Indeed, as will be shown here from microstructural and EPR investigations, high quality cZnS:Mn nanocrystals are obtained by a surfactant-assisted liquid-liquid synthesis reaction of ZnS doped with Mn^{2+} ions, resulting in a self-assembled mesoporous nanomaterial, with a narrow range of nanocrystal sizes, similar in structure to the pure, mesoporous ZnS [10]. Moreover, as expected, the restraining/ordering effect of self-assembling yields a better resolved Electron Paramagnetic Resonance (EPR) spectrum, which helps in the clear identification of three types of isolated Mn^{2+} centers, called $\text{Mn}^{2+}(\text{I})$, $\text{Mn}^{2+}(\text{II})$ and $\text{Mn}^{2+}(\text{III})$, the first consisting of paramagnetic impurity ions localized in the cZnS:Mn nanocrystals, while the other two centers being surface centers.

2. EXPERIMENTAL

The mesoporous cZnS:Mn was synthesized by precipitation in a surfactant-assisted liquid-liquid reaction, at room temperature, by a procedure similar to the one previously employed in the case of undoped mesoporous cZnS [10].

In the present case, the preparation procedure started by adding 0.2 % mol manganese acetate [$\text{Mn}(\text{CH}_3\text{-COO})_2 \cdot 4\text{H}_2\text{O}$] to the solution of zinc acetate [$\text{Zn}(\text{CH}_3\text{COO})_2 \cdot 2\text{H}_2\text{O}$]. The resulting solution was further mixed for another 15 minutes and afterwards co-precipitated with sodium sulphide [$\text{Na}_2\text{S} \cdot 9\text{H}_2\text{O}$], in the presence of the Tween 20 (polyoxyethylene sorbitan monolaurate) surfactant. In the post synthesis steps the precipitate was filtered, washed with bi-distilled water and methanol and dried at 50 °C for 24 hours. The structure of the resulting white crystalline powder was investigated by X-ray diffraction (XRD) and Transmission Electron Microscopy (TEM).

The XRD patterns were recorded on a computer-controlled DRON DART UM2 diffractometer equipped with a graphite monochromatized Cu anode. The spectra were collected both in the low angle ($1.5^\circ < 2\theta < 10^\circ$) and in the wide angle ($5^\circ/10^\circ < 2\theta < 70^\circ$) regions.

The specimens for TEM observations were prepared by crushing the mesoporous cZnS:Mn samples, dispersing the resulting powder in ethanol and dropping it on holey carbon grids. TEM images were obtained with a JEOL 200 CX electron microscope, operating at 200 kV. The images were digitally recorded with the aid of a Keen View CCD camera.

The X (9.8 GHz)-band EPR measurements were performed at room temperature (RT) on a Varian E-line spectrometer upgraded with a Bruker digital EMX-plus console connected to a high sensitivity digital Premium X microwave bridge and cylindrical cavity. The magnet was powered by a Hall controlled ultra stable power supply specially built for the V7000 series 12" electromagnet. The microwave frequency and the magnetic field were measured with an accuracy of 10^{-6} by the frequency counter built in the microwave bridge and the NMR Teslameter (model ER 036TM), respectively. The upgraded spectrometer exhibits a minimum absolute sensitivity of 2.5×10^9 spins/0.1mT, as determined with the weak pitch. The magnetic field at the sample has been calibrated with reference to DPPH and a polycrystalline (CVD grown) diamond sample containing paramagnetic N^0 centers, which exhibit a central narrow EPR line at $g = 2.0024$ [11]. The magnetic field calibration was also tested by setting the magnetic field at a fixed value and determining with the NMR teslameter the magnetic field gradient between its normal position, during the EPR measurements, next to the microwave cavity, and at the sample place, in the magnet center. The two magnetic field calibration tests were found to agree within 0.01 mT. The determination of the spin Hamiltonian parameters has been performed with the computer program EPR-NMR v. 6.4 (Department of Chemistry, University of Saskatchewan, Canada).

The mesoporous ZnS:Mn samples, in the form of a large grained white powder, were put into standard EPR sample tubes of 4 mm o.d. with one end closed, made from pure silica and tightly sealed with plastic caps. The samples were submitted to thermal treatments, for which the plastic cap was removed and the sample tube containing the mesoporous cZnS:Mn was inserted into a universal oven, electronically set at the required temperature within ± 0.5 °C accuracy.

3. RESULTS

3.1. STRUCTURAL CHARACTERIZATION OF THE MESOPOROUS cZnS:Mn

The observed XRD pattern (Fig. 1) of the mesoporous cZnS:Mn nanomaterial exhibits similar features as in the case of pure mesoporous cZnS [10]. At small angles it exhibits a single peak, which is indicative of a sponge-like material with a narrow pore size distribution, but with an irregular arrangement of the pores, a so called worm hole or sponge-like material. As shown in the case of pure mesoporous cZnS [10], the peak at low angles is observed only in the last stage of drying, when the self-assembling of the nanocrystals into a mesoporous structure seems to take place.

At wide angles the XRD pattern exhibits (Fig. 1 – inset) the three broad Miller indexed peaks (111), (220) and (311) of the cubic ZnS structure (JCPDS file no. 05-0566), with the corresponding lattice parameter value of 0.5385 nm. Based on the Scherrer's formula [12], a mean crystallite size of (1.8 ± 0.2) nm was determined from the width of the three peaks. Moreover, considering the resulting d-Bragg correlation distance of 3.6 ± 0.3 nm between the centers of two adjacent pores, as determined from the low angle peak, and assuming the pore walls thickness to be determined by the crystallites size, the pore size mean value of 1.8 ± 0.3 nm was obtained.

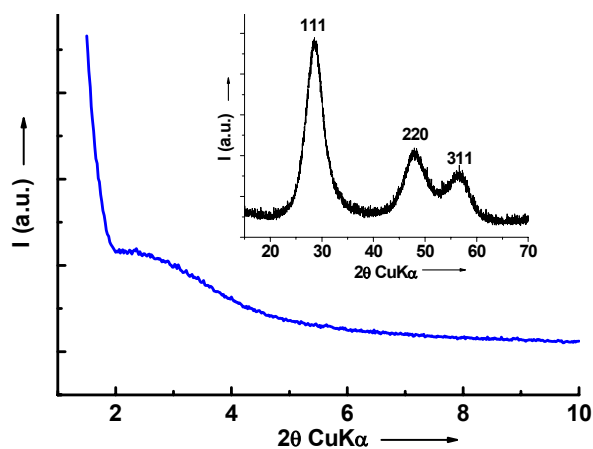


Fig. 1 – The XRD diffractogram of the mesoporous cZnS:Mn sample doped with 0.2 % mol Mn^{2+} in the low angle region. Inset: the wide-angle XRD diffractogram.

The microstructural and morphology investigations of the dried mesoporous cZnS:Mn nanomaterial, performed by conventional – (TEM) – confirm the XRD observations. A characteristic TEM image (Fig. 2a) reveals the mesoporous structure of the specimen with a sponge-like morphology, as previously observed

in pure mesoporous cZnS samples [10]. The pore walls are constituted from cross-linked nm-sized cZnS:Mn crystallites of rather uniform round shapes. The corresponding electron diffraction pattern (Fig. 2b) consists of broad rings, characteristic for a very fine grained material. The diffraction rings can be indexed based on the cubic ZnS structure.

TEM data were further used to determine the size distribution of the cZnS:Mn nanocrystallites. This has been achieved by examining and comparing several TEM images in which the contrast, essential in observing the limits of the crystallites, has been enhanced with the aid of an image processing software. By measuring the diameter/size of 259 nanocrystallites, the calculated average diameter determined by TEM is $d = (2.1 \pm 0.3)$ nm, which reasonably agrees with the (1.8 ± 0.2) nm value determined from XRD measurements. The rather large estimated experimental error results from the difficulty in determining the size of each nanocrystallite in the agglomerates.

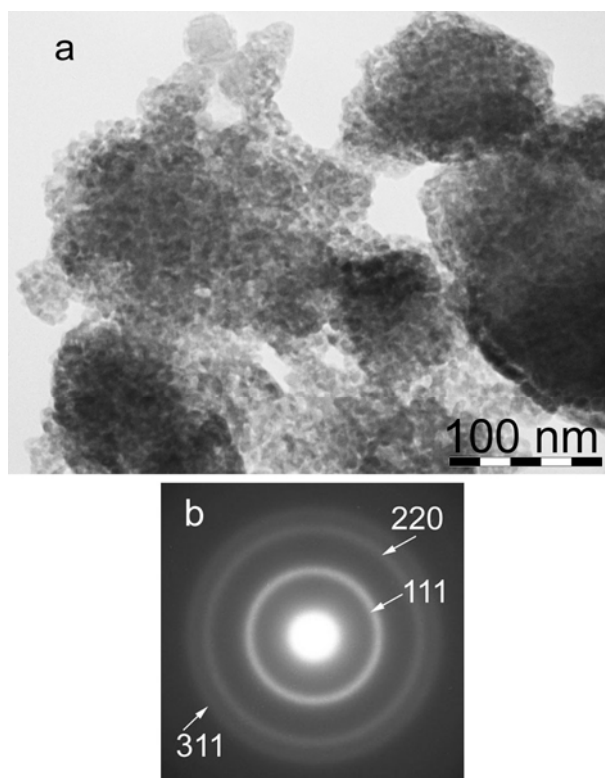


Fig. 2 – a) TEM image revealing the mesoporous morphology of the cZnS:Mn sample. b) The corresponding electron diffraction pattern consisting of broad rings, characteristic for a very fine grained material, which was indexed with the cubic ZnS structure.

3.2. THE EPR INVESTIGATIONS

The EPR spectrum of the as-prepared mesoporous cZnS:Mn (Fig. 3a) exhibits a better resolved pattern compared to similar spectra of nanocrystalline cZnS:Mn powders previously reported in the literature [4–7]. Three sets of six lines, of almost equal intensity, separation and linewidth for each set, can be easily identified in the observed spectrum. Based on the general spectral features [13], as well as on the results of experimental investigations and theoretical evaluations of Mn^{2+} ions in cubic and lower symmetry crystalline powders [14–16], each set of lines was attributed to the six hyperfine components of the central hyperfine allowed ($\Delta M_S = 1/2 \leftrightarrow -1/2$, $\Delta M_I = 0$) transitions from a distinct isolated Mn^{2+} paramagnetic species. The additional set of five pairs of less intense lines observed between the six most intense lines, was attributed to the central forbidden hyperfine transitions ($\Delta M_S = 1/2 \leftrightarrow -1/2$, $\Delta M_I = \pm 1$) of the same center, a well known feature for the Mn^{2+} ions in crystalline powders [16, 17]. The individual spectrum lines attributed to the so called Mn^{2+} (I), Mn^{2+} (II) and Mn^{2+} (III) centers are indicated in Fig. 3 by the corresponding sets of vertical bars.

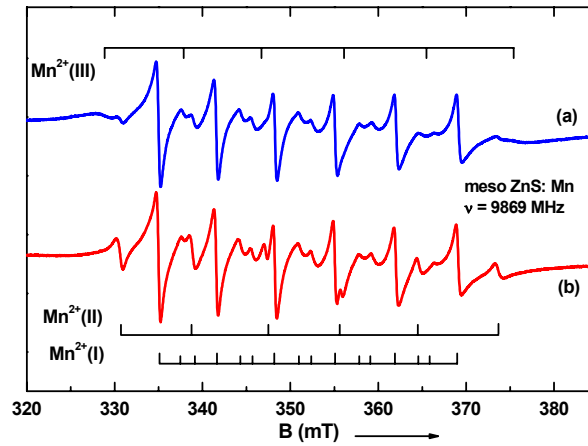


Fig. 3 – The X (9.8 GHz)-band EPR spectrum at room temperature of an “as prepared” mesoporous cZnS:Mn specimen (a) and after being annealed up to 200 °C in air for 15 minutes (b). The transitions from the three identified Mn^{2+} centers are indicated by vertical lines.

The EPR spectrum of each type of center can be described by the spin Hamiltonian (SH) with usual notations [13]:

$$H = \mu_B \vec{S} \hat{g} \vec{B} + \vec{S} \hat{A} \vec{I} + \mu_N g_N \vec{B} \vec{I} + \frac{a}{6} \left[(S_x^4 + S_y^4 + S_z^4) + \frac{1}{5} S(S+1)(3S^2 + 3S - 1) \right] + D \left[S_z^2 - \frac{1}{3} S(S+1) \right]. \quad (1)$$

The first two terms in (1) describe the interaction of the electron spin ($S = 5/2$) with the external magnetic field and the nuclear spin ($I = 5/2$) of the ^{55}Mn (100 % natural abundance) isotope, respectively. The third one corresponds to the nuclear Zeeman interaction of the ^{55}Mn nucleus. The last two terms are the zero field splitting (ZFS) terms, which describe the interaction of the unpaired electron spin with the cubic and axial components of the local crystal field, respectively. These terms are responsible for the anisotropy of the EPR spectrum of the individual cZnS:Mn crystallites.

The EPR spectrum from Mn^{2+} ions in an individual cubic ZnS crystallite consists of 30 hyperfine allowed ($\Delta M_S = \pm 1$, $\Delta M_I = 0$) and up to 50 hyperfine forbidden ($\Delta M_S = \pm 1$, $\Delta M_I = \pm 1$) transitions of much smaller intensity. However, in the case of the latter ones, due to line broadening effects, only the central 10 transitions ($\Delta M_S = 1/2 \leftrightarrow -1/2$, $\Delta M_I = \pm 1$) are visible at high magnifications [17]. In the experimental spectrum, which is the result of the overlap of the EPR spectra of Mn^{2+} ions from individual nanocrystallites with various orientations in the magnetic field, the strongly anisotropic ($\Delta M_S = \pm 1/2 \leftrightarrow \pm 3/2$ and $\pm 3/2 \leftrightarrow \pm 5/2$, $\Delta M_I = 0, \pm 1$) allowed and forbidden transitions are smeared out by the spatial averaging combined with the strong line broadening effect due to the crystal field fluctuations related to the higher lattice disorder in the nanocrystalline material. Thus, only the 6 intense lines corresponding to the isotropic central hyperfine allowed transitions and the less intense 10 hyperfine forbidden transitions lying in pairs between the former ones are visible. This situation happens in the case of the $\text{Mn}^{2+}(\text{I})$ centers. Due to the larger linewidth and smaller intensity, it is not possible to distinguish the hyperfine forbidden transitions in the case of the overlapping spectra of the $\text{Mn}^{2+}(\text{II})$ and $\text{Mn}^{2+}(\text{III})$ centers.

As shown by analytical perturbation calculations [14, 18, 19], both ZFS terms in (1), characterized by the parameters D and a , have a negligible third order effect on the line positions of the central allowed transitions. Therefore, it is possible to determine from fitting the central allowed transition fields only the g and A parameters of the three centers. The resulting values are presented in Table 1 in comparison with early reported data. The same analytical calculations [14, 18, 19] have shown that the positions of the central forbidden transitions are influenced in the second order by the axial ZFS term. Therefore, in the case of the $\text{Mn}^{2+}(\text{I})$ centers it was possible to determine the D parameter, which is the largest of the two ZFS parameters, by fitting both central allowed and forbidden transition fields. Because the g and A values of this center were found to be very close to those reported in the case of substitutional Mn^{2+} ions in cubic ZnS single crystals [17], we took in our calculations the single crystal value of the cubic ZFS parameter $a = 7.987 \times 10^{-4} \text{ cm}^{-1}$.

The resulting SH parameter values and the experimental peak to peak derivative linewidth ΔB are presented in Table 1 in comparison with the previously reported data (where available). They offer the basis for identifying the localization of the Mn^{2+} ions in the nanocrystalline cZnS:Mn. In the case of the $\text{Mn}^{2+}(\text{I})$ center,

the similar values of the g and A parameters with the corresponding highly accurate values recently reported in cubic ZnS single crystals [17], lead to the conclusion that the $\text{Mn}^{2+}(\text{I})$ centers, representing about 25% of the isolated Mn^{2+} ions contained in the mesoporous cZnS:Mn , consist of Mn^{2+} ions at substitutional Zn^{2+} sites, which in the unperturbed ZnS crystal lattice exhibit a local T_d symmetry. However, the presence of an additional small local axial crystal field distortion at the Mn^{2+} ions, characterized by the $|D| = 45 \times 10^{-4} \text{ cm}^{-1}$ value, which had to be considered in order to explain the observed line positions, strongly suggests the presence of a local distortion. The presence of a local axial crystal field component is also supported by the rather large increase in the ratio of the central forbidden to allowed transitions, between 0.04 and 0.15 as compared to the average value of 10^{-3} in the case of cubic ZnS single crystals [17]. Such increase in the intensity of the central forbidden transitions has been previously observed in Mn^{2+} doped molecular sieves and polycrystals and explained by the presence of local non-cubic crystal field components [13–15]. The source of the local non-cubic crystal field components, which can be due either to local lattice distortions related with the presence of a neighboring impurity or to a lattice defect, remains to be investigated.

Table 1

The spin Hamiltonian (SH) parameters, determined in the present work by transition fields fitting, and the peak to peak EPR linewidth values ΔB (in mT) of the Mn^{2+} centers in mesoporous cZnS:Mn , compared with previously reported values in cubic ZnS single crystals and nanocrystals. The D and A parameters are given in $[10^{-4} \text{ cm}^{-1}]$ units

Center/host	g	A	$ D $	ΔB	References
$\text{Mn}^{2+}(\text{I})/\text{mezo cZnS}^*$	2.0020 ± 0.0002	-63.9 ± 0.4	45 ± 8	0.4	This work
NC1 / nano cZnS	2.003	64.5			[4]
SI / nano cZnS	2.0010	- 63.9	1.0	0.9	[5]
Center I / nano cZnS	2.0024	-64.5	91.0	0.7	[6]
Center Ib / nano ZnS	$g_{\perp} = 2.0075$ $g_{\parallel} = 2.004$	$ A_{\perp} = 63.8$ $ A_{\parallel} = 65.2$	37.4; $ E = 12.5$	0.6	[7]
Mn^{2+} in cZnS single crystals *	2.0022	-63.88	0	0.1-0.04	[17]
$\text{Mn}^{2+}(\text{II})/\text{mezo cZnS}$	2.0009 ± 0.0005	-80.6 ± 0.5		0.6	This work
Center II / nano cZnS	2.0013	- 84.13	160	1.08	[6]
Center Ih / nano cZnS	$g_{\perp} = 2.006$ $g_{\parallel} = 2.003$	$ A_{\perp} = 79.5$ $ A_{\parallel} = 84$	373.9; $ E = 124.6$	0.6	[7]
$\text{Mn}^{2+}(\text{III})/\text{mezo cZnS}$	2.000 ± 0.002	-87.0 ± 1.0		1.5	This work
NC2 / nano cZnS	2.001	89	500-1000		[4]
SII / nano cZnS	2.0010	- 90.0	1.0	4.7	[5]

(*) Cubic ZFS parameter value $a = 7.987 \times 10^{-4} \text{ cm}^{-1}$.

The larger values of the hyperfine splitting parameter A observed for the other two $\text{Mn}^{2+}(\text{II})$ and $\text{Mn}^{2+}(\text{III})$ centers suggest changes in the bonding and/or

coordination at the Mn^{2+} ion. One expects the Mn^{2+} ion in both centers to be subjected to a larger non cubic crystal field than in the case of the $\text{Mn}^{2+}(\text{I})$ center, which could also explain, at least partially, their increased spectral linewidths. Unfortunately, due to the difficulty in observing the corresponding forbidden transition doublets, the determination of the ZFS parameter could not be done as in the case of the $\text{Mn}^{2+}(\text{I})$ centers by line position fitting procedures with the available X-band EPR data. Such determination requires additional data from multifrequency EPR measurements and line shape analysis with sophisticated computer programs, which are underway.

Additional information concerning the structure of the $\text{Mn}^{2+}(\text{II})$ and $\text{Mn}^{2+}(\text{III})$ centers has been obtained from the analysis of pulse annealing experiments. In such experiments, the EPR sample tube containing the mesoporous cZnS:Mn powder has been annealed in air for 15 minutes, in steps of 25 degrees, from $+50^\circ\text{C}$ up to $+200^\circ\text{C}$, and after each temperature step the EPR spectrum was recorded at RT. One should mention that the variation in the amplitude of the EPR lines from the different Mn^{2+} centers, for constant linewidth, is proportional to changes in their concentration. We have observed for $T_{\text{ann}} > 125^\circ\text{C}$ an increase in the concentration of the $\text{Mn}^{2+}(\text{II})$ centers, accompanied by a corresponding decrease in the concentration of the $\text{Mn}^{2+}(\text{III})$ centers. Meanwhile, no significant changes in the concentration of the $\text{Mn}^{2+}(\text{I})$ centers have been noticed, as expected for impurity ions localized inside the cZnS:Mn nanocrystallites. Fig. 3b presents the EPR spectrum measured after pulse annealing the sample up to $T_{\text{ann}} = +200^\circ\text{C}$, which shows the almost complete decay of the $\text{Mn}^{2+}(\text{III})$ centers accompanied by a proportional increase in the concentration of the $\text{Mn}^{2+}(\text{II})$ centers. Based on these results one can assume with high certainty that in the $\text{Mn}^{2+}(\text{II})$ and $\text{Mn}^{2+}(\text{III})$ centers the Mn^{2+} ions are localized in the outer layer / at the surface of the cZnS:Mn nanocrystallites. Moreover, the pulse annealing experiments show that the Mn^{2+} ion of the $\text{Mn}^{2+}(\text{III})$ center is very likely bound to an adsorbed water molecule, which is lost by heating, resulting in the $\text{Mn}^{2+}(\text{II})$ center.

4. CONCLUSIONS

Mesoporous cZnS:Mn self-assembled from nanocrystals of cubic ZnS:Mn of 2 nm average size, as determined from XRD and TEM measurements, has been prepared by a surfactant-assisted liquid-liquid reaction. The expected ordering effect of self-assembling explains the tighter size distribution of the cZnS:Mn nanocrystals (Fig. 2c) compared with available data on cZnS nanopowders [6, 7]. Examination of the Table 1 reveals that in the case of the three Mn^{2+} ions with different localizations in the investigated mesoporous cZnS:Mn the EPR linewidth values are smaller compared to similar Mn^{2+} centers reported in the literature. The better resolved EPR spectrum, with narrower component lines, did allow us to determine the SH parameters g and A for the three $\text{Mn}^{2+}(\text{I})$, $\text{Mn}^{2+}(\text{II})$ and $\text{Mn}^{2+}(\text{III})$ paramagnetic centers by fitting the 6 central line positions with the computed

values resulting from the diagonalization of the SH given in (1). Moreover, in the case of the Mn^{2+} (I) center it has been also possible to determine the ZFS parameter D value by including in the analysis the observed 10 central forbidden transitions as well. Comparing the resulting SH parameters with the corresponding values for Mn^{2+} ions in cubic ZnS single crystals and nanocrystals reported in the literature (Table 1), one concludes that the majority of the Mn^{2+} impurity ions, labeled as Mn^{2+} (I) centers, are substitutionally localized at isolated Zn^{2+} sites in the ZnS nanocrystallites lattice, being subjected to a small local distortion. For the moment its origin is still unclear and needs further investigations. More accurate determinations of the SH parameters based on the analysis of spectra recorded at different microwave frequencies with line shape fitting procedures, which are underway, may shed further light on this subject.

Based on the observed values of the g and A SH parameters and their specific behavior during the thermal treatment we found out that, in the case of the Mn^{2+} (II) and Mn^{2+} (III) centers, the Mn^{2+} ions are localized at the surface of the cZnS:Mn nanocrystallites. The available data do not allow the determination of the role played by the surfactant employed in the preparation of the mesoporous cZnS:Mn in the formation and structure of the two centers.

Acknowledgements. The present research was performed in the frame of the project PN-II-ID-PCE no. 523/2009 financed by the Romanian Ministry of Education and Research through UEFISCSU. We thank D. Zarnescu for excellent experimental assistance.

REFERENCES

1. R. N. Bhargava and D. Gallagher, *Phys. Rev. Lett.*, **72**, 416 (1994).
2. H. Hu and W. Zhang, *Opt. Materials*, **28**, 5, 536 (2006).
3. A. A. Bol and A. Meijerink, *Phys. Rev.*, **B 58**, R15997 (1998).
4. T. A. Kennedy, E. R. Glaser, P. B. Klein and R. N. Bhargava, *Phys. Rev.*, **B 52**, R14356 (1995).
5. P. H. Borse, D. Srinivas, R. F. Shinde, S. K. Date, W. Vogel and S. K. Kulkarni, *Phys. Rev.* **B 60**, 8659 (1999).
6. T. Igarashi, M. Ihara, T. Kusunoi, K. Ohno, T. Isobe and M. Senna, *J. Nanoparticle Res.*, **3**, 51 (2001).
7. P. A. Gonzalez Beermann, B. R. McGarvey, B. O. Skadtchenko, S. Muralidharan and R. C. W. Sung, *J. Nanoparticle Res.*, **8**, 235 (2006).
8. D. J. Norris, Nan Yao, F. T. Charnok and T. A. Kennedy, *Nano Letters*, **1**, 1, 3 (2001).
9. J. Yang, J. J. Peng, R. Zhou, F. Peng, H. Wang, H. Yu and J. Y. Lee, *Nanotechnology*, **19**, 255603 (2008).
10. L. C. Nistor, C. D. Mateescu, R. Birjega and S. V. Nistor, *Appl. Phys.*, **A91**, 295 (2008).
11. I. I. Vlasov, V. G. Ralchenko, A. V. Komich, S. V. Nistor, D. Schoemaker and R. A. Khmel'nitskii, *Phys. Stat. Sol.*, **A 181**, 83 (2000).
12. B. D. Cullity and S. R. Stock, *Elements of X-ray Diffraction*, Pearson Education, 3rd ed., 2003.
13. A. Abragam and B. Bleaney, *Electron Paramagnetic Resonance of Transition Ions*, Clarendon Press, Oxford, 1970.
14. A. Nicula, I. Ursu and S. V. Nistor, *Rev. Roum. Phys.*, **10**, 229 (1965).
15. J. Rubio O., E. Munoz P., J. Boldu O., Y. Chen and M. M. Abraham, *J. Chem. Phys.*, **70**, 633 (1979).
16. S. K. Misra, *Physica*, **B203**, 193 (1994).
17. S. V. Nistor and M. Stefan, *J. Phys.: Condens. Matter*, **21**, 145408 (2009).
18. S. V. Nistor, *Rev. Roum. Phys.*, **13**, 539 (1968).
19. L. Giurgiu and S. V. Nistor, *Rev. Roum. Phys.*, **14**, 683 (1969).